Geophysical Journal International

Geophys. J. Int. (2024) **239,** 276–291
Advance Access publication 2024 August 05
GJI General Geophysical Methods

https://doi.org/10.1093/gji/ggae272

Comparing geophysical inversion and petrophysical measurements for northern Victoria Land, Antarctica

Maximilian Lowe [1,2] Tom Jordan [1] Jörg Ebbing [3] Nikola Koglin [4] Antonia Ruppel [4] Max Moorkamp [5,6] Andreas Läufer [4] Chris Green [7] Jonas Liebsch [3,8] Mikhail Ginga [3] and Robert Larter [1]

[1] *NERC British Antarctic Survey, Palaeo Environments, Ice Sheets and Climate Change, CB3 0ET Cambridge, United Kingdom. E-mail: maxwe32@bas.ac.uk*
[2] *University of Edinburgh, School of Geosciences, EH8 9XP Edinburgh , United Kingdom*
[3] *Kiel University, Institute of Geosciences, 24118 Kiel, Germany*
[4] *Federal Institute for Geosciences and Natural Resources, Polar Geology, 30655 Hannover, Germany*
[5] *Ludwig Maximilian University of Munich, Department of Earth and Environmental Sciences, 0333 München, Germany*
[6] *Technical University of Berlin, Institute of Applied Geosciences, 10587 Berlin, Germany*
[7] *University of Leeds, School of Earth and Environment, LS2 9JT Leeds, United Kingdom*
[8] *University of Iceland, Institute of Earth Sciences, 102 Reykjavik, Iceland*

Accepted 2024 July 26. Received 2024 July 12; in original form 2024 March 20

SUMMARY

Bedrock geology from Antarctica remains largely unknown since it is hidden beneath thick ice sheets. Geophysical methods such as gravity and magnetic inverse modelling provide a framework to infer crustal rock properties indirectly in Antarctica. However, due to limited availability of rock samples, validation against direct geological information is challenging. We present a new rock property catalogue containing density and susceptibility measurements on 320 rock samples from northern Victoria Land. This catalogue is used to assess the reliability of local and regional scale inverse results, including a new local high resolution magnetic inversion in the Mesa Range region and a previously published regional scale joint inversion of gravity and magnetic data in northern Victoria Land and the Wilkes Subglacial Basin. We compare our density and susceptibility measurements to global and local measurements from the literature to access the correlation to rock types and geological units. Furthermore, the measured values are compared against inverted values. The close correspondence between inverted and measured rock properties allows us to predict locations of rock types where currently such information is missing. The utility of measured susceptibility and density relationships for interpreting inversion output provides a strong incentive to incorporate local rock samples into geophysical studies of subglacial geology across Antarctica.

Key words: Gravity anomalies and Earth structure; Antarctica; Magnetic anomalies: modelling and interpretation; Rock and mineral magnetism; Joint inversion.

1 INTRODUCTION

One of the largest challenges currently in solid earth research in Antarctica is reliable imaging of subglacial geology and crustal properties. The overwhelming majority of Antarctica's geology is hidden beneath thick ice sheets limiting direct geological information to ice free regions at the coast, high mountain ranges and isolated nunataks. Geological structures and subice solid Earth properties are therefore inferred most commonly from geophysical approaches: airborne gravity, magnetic and radar measurements (e.g. Goodge & Finn 2010; Ferraccioli *et al.* 2011; Riedel *et al.* 2012; Jordan *et al.* 2013, 2022, 2023; Aitken *et al.* 2014; Mieth & Jokat 2014; Mieth *et al.* 2014; Gibson *et al.* 2015; Ruppel *et al.* 2018). The caveat is that the complexity of geological structures, which can be inferred, depends on the flight line spacing and altitude of the airborne surveys. High resolution surveys with tight flight line spacing (≤500 m) are rare in Antarctica and where conducted are usually limited to magnetic measurements over local (10 s of km) surveys (e.g. Wilson *et al.* 2007; Damaske *et al.* 2014; Ghirotto *et al.* 2023).

Complementary to geophysical crustal forward modelling, magnetic-only and joint inversions of gravity and magnetic data have been successfully applied to different environments and scales to image crustal properties in terms of density and susceptibility distribution beneath the Antarctic ice sheet (e.g. Lösing *et al.* 2022; Jordan *et al.* 2023; Morales-Ocaña *et al.* 2023; Lowe *et al.* 2023a).

A remaining challenge is to directly link geological information with geophysical models. Petrophysical rock properties, namely susceptibility and density, allow linking of these observations and cross-validation of hypotheses arising from geological or geophysical interpretation.

Remaining open questions are how well inverted petrophysical parameters correspond to laboratory derived petrophysical parameters measured on Antarctic rock samples, whether it is possible to separate and classify subglacial rock types based on inverted petrophysical properties, and what the possible limitations are. The lack of linkage between Antarctic geophysical models and petrological data arises from a lack of density and susceptibility measurements on the same rock samples in the literature and therefore, Antarctic models are often validated against catalogues of global rock properties or rock samples from Australia (e.g. Lösing *et al.* 2022).

To answer these questions, we present a petrophysical catalogue containing 320 measurements of susceptibility and density values. Those measurements are performed on rock samples from northern Victoria Land (nVL), which are archived by the German Federal Institute for Geosciences and Natural Resources (BGR) from over 40 yr of expeditions to nVL. Additionally, we present a new high resolution local susceptibility inversion of the Mesa Range area in nVL based on a helicopter magnetic survey with a 500 m line spacing conducted by BGR in the 2009–2010 Antarctic season (Damaske *et al.* 2014). Gravity measurements on a comparable resolution do not exist for the local study area. Instead, we discuss additionally a coupled inverted susceptibility and density crustal distribution model, on a regional scale in nVL and the Wilkes Subglacial Basin (WSB), which has been previously published (Lowe *et al.* 2023b). This model is based on a joint inversion of gravity and magnetic airborne data, which accommodates the gravity resolution and therefore adds an additional dimension that fully utilises the advantages of joint inversion of potential fields, albeit with a coarser grid resolution.

1.1 Regional geology

NVL is located at the Pacific end of the Transantarctic Mountains (TAM), one of the largest non-collisional mountain chains worldwide (Fig. 1). The basement formed by accretionary processes at the East Gondwana active continental margin during the late Ediacaran–early Palaeozoic Ross Orogeny e.g. (Goodge 2020). Geologically the TAM consists of the western and inboard polymetamorphic and magmatic Wilson Terrane, the central volcanic and clastic Bowers Terrane, and the eastern turbiditic Robertson Bay Terrane. The metamorphic basement of the Wilson Terrane comprises low- to high-grade (up to granulite-facies) metamorphic rocks, involving, for example the Wilson metamorphic and polymetamorphic complexes, the Berg Group or the Wilson Schists, as indicated in Fig. 2. The metamorphic country rocks are intruded by the voluminous Granite Harbour Intrusive (GHI) Complex (here also including the anatectic Oates Coast granitoids listed in Fig. 2). The majority of the plutonic rocks consist of granitoids with subordinate intermediate to mafic varieties as well as some ultramafics. The Bowers Terrane comprises very low- to low-grade metavolcanics and associated metavolcaniclastics, which formed in an island arc or fore-/backarc tectonic setting and grade into molasse-type clastic metasedimentary rocks (Bowers Supergroup, Figs 1 and 2). The outboard Robertson Bay Terrane consists of mostly distal turbidites of the Robertson Bay Group deposited furthest from the continent interior (Figs 1 and 2). The Wilson-Bowers terrane boundary is defined by the strongly deformed Lanterman-Mariner Fault Zone in the Lanterman Range and along the western margin of Mariner Glacier, whereas the Millen Schist Belt represents the boundary between the Bowers and Robertson Bay terranes. Post-Ross geology is characterized by the mid-Palaeozoic felsic Admiralty Igneous Complex comprising the Admiralty granitoids and the Gallipoli volcanics. They are unconformably overlain by late Palaeozoic to early Jurassic clastic Beacon Supergroup and sills and lavas of the Jurassic Ferrar Supergroup, that is Ferrar Dolerite and Kirkpatrick Basalt including the volcaniclastic Exposure Hill-type deposits (e.g. GANOVEX Team 1987; Elliot *et al.* 2021). Youngest rocks in the region involve Cenozoic alkaline to peralkaline magmatic rocks of the McMurdo Igneous Complex, related to West Antarctic rifting, and glacial sediments (Kyle & Cole 1974; Kyle 1990; Rossetti *et al.* 2000; Giordano *et al.* 2012).

2 METHOD: PETROPHYSICAL MEASUREMENT AND INVERSION

We conducted susceptibility and density measurements on 320 rock samples from nVL. Susceptibilities of the rock samples were measured using a handheld KAPPAMETER KM-7 (Pocket Magnetic Susceptibility Meter). For each rock sample eight repeat measurements were performed on different flat and, if possible, fresh surfaces. Density was measured by weighing the dry sample and dividing this by the volume. The volume of the sample was determined by suspending it from a string in a water container, allowing it to achieve equilibrium. The string offsets the difference of gravitational and buoyancy forces acting on the sample. Consequently, the buoyancy force acting on the sample can be quantified using a scale positioned at the base of the container. Density is then calculated using the density of water, the weight of the dry sample and the weight of displaced water (eq. 1).

$$\text{Density } \rho = \frac{\text{Weight}_{\text{rock}}\ \text{Density}_{\text{water}}}{\text{Weight}_{\text{displaced Water}}}. \quad (1)$$

Inversion of magnetic data alone is carried out using the open-source scientific code JIF3D. The joint inversion model, also carried out in JIF3D, is discussed in depth in Lowe *et al.* (2023b). The theoretical background is given in detail in (Moorkamp *et al.* 2011; Moorkamp 2021, 2022). Therefore, we restrict the description here to a description of the objective function and its regularisation parameters. The objective function for the joint inversion Φ_{joint}, as described in Lowe *et al.* (2023b), has five terms (eq. 2). Two misfit terms represent the difference between the gravity and magnetic field responses of the model and the observed fields. Two regularization parameters relate to the two petrophysical quantities (density and susceptibility). JIF3D uses a finite difference approximation to the spatial gradient for regularisation, meaning differences in values between adjacent cells are penalized. Therefore, a higher regularization value leads to a smoother model with less variation. A full description of the regularisation parameter can be found in Moorkamp *et al.* (2011). The last term is the Variation of Information parameter, which enforces a coupling between both physical quantities (Moorkamp *et al.* 2011; Moorkamp 2021, 2022; Lösing *et al.* 2022; Lowe *et al.* 2023b).

$$\Phi_{joint} = \Phi_{d,grav} + \Phi_{d,mag} + \lambda_1\Phi_{reg,\rho} + \lambda_2\Phi_{reg,sus} + \lambda_3\Phi_{VI}\ , \quad (2)$$

where $\Phi_{d,grav}$ and $\Phi_{d,mag}$ are the root-mean-square (RMS) misfit between observed and inverted gravity and magnetic data, respectively, $\Phi_{reg,\rho}$ and $\Phi_{reg,sus}$ are regularisation parameters, and Φ_{VI} is

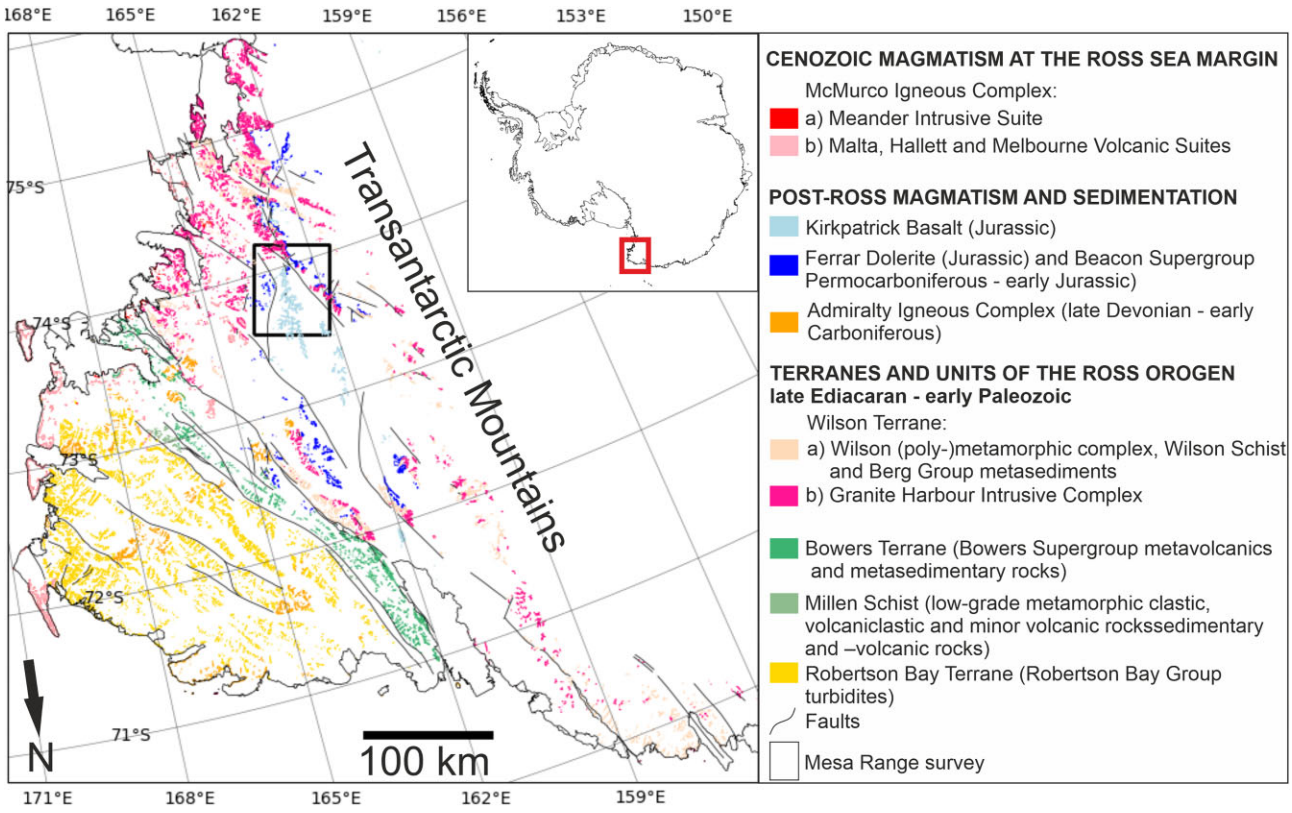

Figure 1. Geological map of northern Victoria Land and Oates Land. Geological data taken from (Cox *et al.* 2023b). Based on (Roland *et al.* 2002; Läufer *et al.* 2011; Pertusati *et al.* 2016). Inset shows study location (red box) in Antarctic context.

the coupling term based on the variation of information approach (Moorkamp *et al.* 2011; Lösing *et al.* 2022; Moorkamp 2022).

For the local magnetic inversion over the Mesa Range, we use the joint inversion algorithm described above but with the coupling weights and all terms associated with the gravity data set to zero. The subsurface was discretized into a mesh with a horizontal cell size of 250 m and a vertical cell size of 100 m at the surface, which increased by a constant factor of 1.1 for each layer with depth to account for decreasing resolution of potential field data with depth and to limit the computational load (Fig. S4). This results in a vertical thickness of the upper most cell layer of 100 m, while the layer beneath has a thickness of 110 m and so on. The deepest layer of cells has a thickness of 3400 m at a model depth of 32 701 m. This approach prevents the inversion from producing high frequency structures at depth, which cannot be resolved by the measured input data. For the upper boundary surface, bedrock information from BedMachine Antarctica (Morlighem *et al.* 2020) was used (Fig. S3), while for the lower boundary surface, Curie Point Depth (CPD) estimates from (Lowe *et al.* 2023c) are used (Fig. S2a). The Curie Point describes the Curie temperature of around 580 °C, the temperature at which minerals that dominate the magnetic characteristics of crustal rocks lose their magnetic properties (Haggerty 1978; Telford *et al.* 1990; Blakely 1996; Núñez Demarco *et al.* 2020). Moreover, the inversion meshes are extended laterally with a 20 per cent buffer around the target area to reduce edge effects. The regularisation for the susceptibility is set to a value of 10. Supporting information provides alternative runs with varying regularisation values (Figs S5, S6 and S7). Further parameters for the local inversion are given in Table 1.

The regional joint inversion model (Lowe *et al.* 2023a) is based on airborne gravity and magnetic data (Reitmayr *et al.* 2003; Scheinert *et al.* 2016; Golynsky *et al.* 2018; Zanutta *et al.* 2018; Figs S1a and b). The joint inversion model is also confined to the upper boundary condition defined by bedrock topography data from BedMachine Antarctica (Morlighem *et al.* 2022), while the boundary condition for the base of the model differs. For the susceptibility model the CPD values (Fig. S2a; Lowe *et al.* 2023c) are used again as boundary condition while Moho depths (Fig. S2b; Pappa *et al.* 2019a) are used for the density model.

3 RESULTS

3.1 Laboratory-measured susceptibility and density values

Susceptibility and density measurements were conducted on 320 rock samples from nVL including 248 rock samples stored in the National Polar Sample Archive (NAPA) in Berlin-Spandau, Germany and 72 samples stored at the BGR in Hannover, Germany (Fig. 2). The samples were pre-classified on the basis of geological formation (Fig. 2a) and rock types (Fig. 2b) by the sample collectors during the GANOVEX field activities. The location of the samples shows a bias towards the GANOVEX focus (Figs 2a and b). Regardless, geological formations from across the whole of nVL are represented. In general, metamorphic and sedimentary rocks exhibit low susceptibility, while higher susceptibilities were measured for plutonic and volcanic rocks (Figs 2c, e, 3a and c). Susceptibility measurements of granitoids from the GHI complex (Fig. 3a) show a low mean and median value but include some

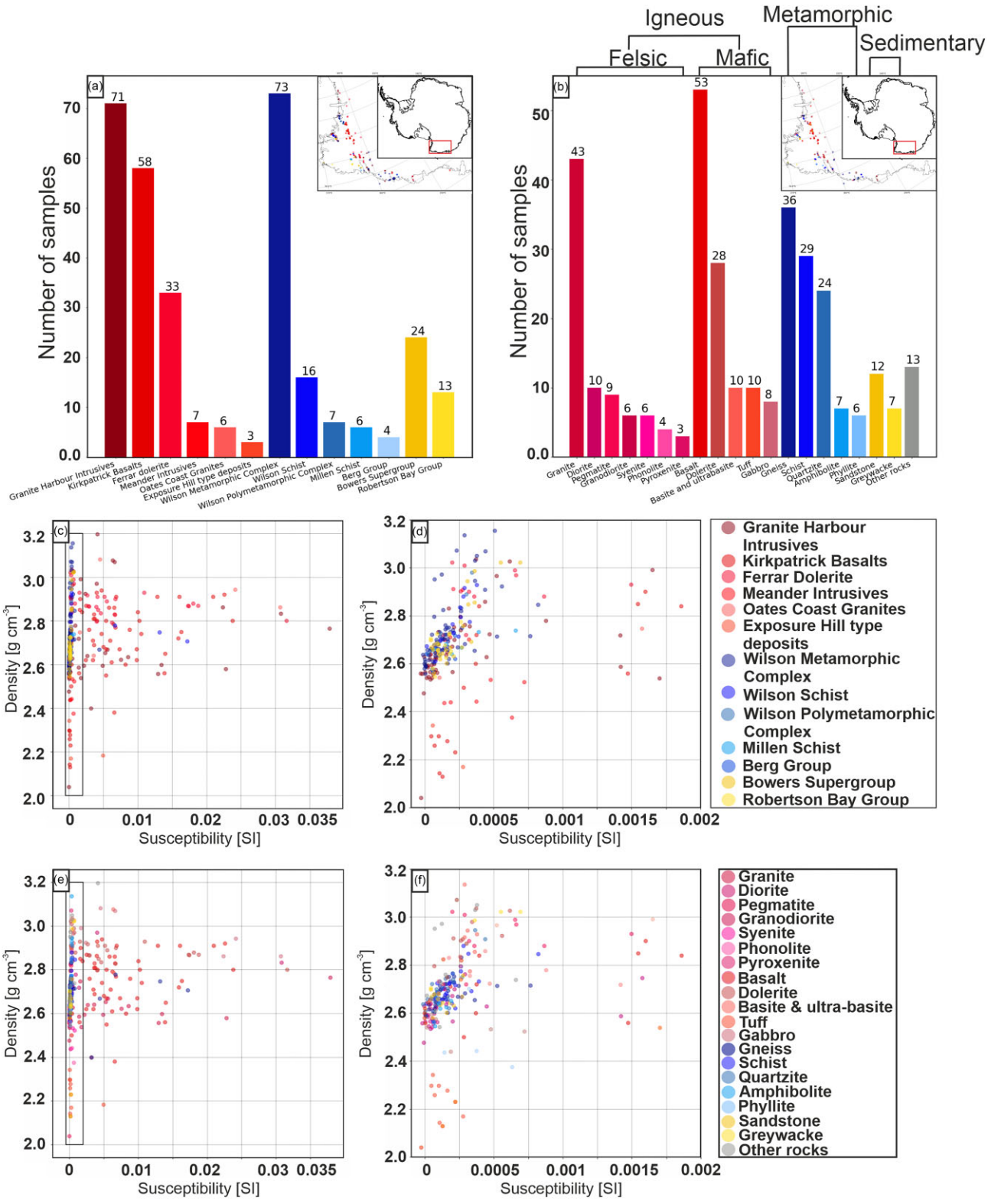

Figure 2. (a) Histogram of measured rock samples and location plot classified by geological formation. (b) Histogram of measured rock samples and location plot classified by rock type. (c) Susceptibility and density cross plot of measured rock samples classified by geological formation. (d) Zoomed in cross plot to low susceptibility range indicated in (c). (e) Susceptibility and density cross plot of measured rock samples classified by rock type. (f) Zoomed in cross plot to low susceptibility range indicated in (e).

Table 1. Inversion parameters. Inclination and declination are calculated for the for the midpoint and the acquisition date of the survey using DGRF calculator implemented in Oasis Montaj (Geosoft).

Regularization susceptibility	10
Error magnetics [nT]	10
Min./Max susceptibility [SI]	±0.1
Magnetic field strength [nT]	64 411
Inclination [Rad]	−1.4566
Declination [Rad]	2.2756
Maximum depth of susceptibility variation	CPD
Observation height	Flight elevation

outliers with high susceptibility values. Outliers are defined as >1.5 times the interquartile ranges.

Gabbros from the Oates Coast Granites and GHI complex followed by Kirkpatrick basalt (KPB) and Ferrar dolerites (FD) show the largest measured susceptibility ranges (ignoring outliers, Figs 3a and c).

Density measurements show larger variation across the formations (Fig. 3b). Distinct clusters of density values are evident for the FD, KPB and GHI complex, which are the dominant geological formations in the Mesa Range area (Fig. 3b). This difference is even stronger when considering the dominant rock types for each formation: dolerites for the FD (mean 2.88 g cm^{-3}), basalt for the KPB (mean 2.75 g cm^{-3}, excluding the lighter Tuff samples) and granites for GHI complex (mean 2.6 g cm^{-3}). The differences in susceptibility are more nuanced between KPB and FD with a mean value of 0.006 SI for FD and 0.0069 SI for KPB, while the median shows a larger difference with values of 0.003 SI for FD and 0.005 SI for KPB (Figs 3a and c). Granites exhibit significantly lower mean and median susceptibility values (mean: 0.002 SI median: 8.12e-05 SI) compared to basalts and dolerites (Fig. 3c).

The FD, KPB and GHI complex show significant outliers in both susceptibility and density. The large range of overlapping density and susceptibility values including outliers does highlight the need for caution when attributing characteristic density and susceptibility values to specific rock types (Fig. 3). Nevertheless, the combination of susceptibility and density measurements on the same rock samples decreases the uncertainty in clustering rocks based on those petrophysical properties. Our new density measurements are broadly in line with previous density measurements on rock samples from nVL (e.g. Barrett & Froggatt 1978), while the susceptibility measurements for the GHI complex are broadly in line with susceptibility values reported in (Bozzo *et al.* 1992, 1995).

3.2 Comparison of the petrophysical measurements to literature values

Density and susceptibility measurements are important to validate geophysical models. Both petrophysical quantities are reported in the literature for Antarctic rock samples, however, usually density and susceptibility values are reported separately (e.g. Maslanyj *et al.* 1991; Bozzo *et al.* 1992, 1995; Sanchez *et al.* 2021). Due to the lack of Antarctic rock outcrops petrophysical measurements on rock samples from Australia (Barlow 2004) and the Indian shield (Subrahmanyam & Verma 1981) have previously been used to validate geophysical models (e.g. Lösing *et al.* 2022). Selected rock types of the petrophysical catalogue from this study are therefore compared to existing literature values to test the validity of this assumption. An obstacle to compare our measurements to literature values is that often the petrophysical measurements are only reported as a mean value for the data set, sometimes a standard deviation is given as well. Therefore, we plot the reported mean values and where possible the standard deviation on top of the boxplots of our petrophysical catalogue (Figs 4 and 5). An exception is the Antarctic-wide PetroChron data set (Sanchez *et al.* 2021), which is a full data set. Therefore, it is possible to plot boxplots for the PetroChron data set as well, which allows the best possible comparison between both data sets (Fig. 5).

Susceptibility values measured in this study and literature values are overall in good agreement. Some reported mean values for granites, GHI, Amphibolite and FD from the literature fit the mean values of this study. However, there are exceptions to this observation. Most prominent, perhaps, are the mean susceptibilities reported for gabbros from the Antarctic peninsula. The mean values are significantly higher and even outside the maximum of the box plot for the nVL rock samples from this study. Some of the mean susceptibility reported for granite rock samples from the Antarctic Peninsula and the Indian shield show significant high susceptibilities outside the boxplot for nVL and are only matched by outliers from nVL. Similar behaviour is observed for Amphibolite and Gneiss. Overall, susceptibility measurements on rock samples from nVL (Bozzo *et al.* 1992, 1995; Ohneiser *et al.* 2015) seem to agree best with our measurements conducted on rock samples from nVL (Fig 4). This shows that there is a geographical variation, that subsequently illustrates the need for caution if rock catalogues including rock samples from geographically distant locations, even other continents, are used for validation.

Mean densities from this study are in strong agreement with density estimations on Antarctic rock samples from the PetroChron data set (Sanchez *et al.* 2021, Fig. 5). A discrepancy between the two data sets is evident for basaltic rocks. Overall, the density range for basalt from PetroChron is tighter. However, the minimum and maximum illustrated by the boxplot overlap, especially when considering the outliers for the PetroChron data set. The outliers might indicate geographical clusters, which seems to align with the measurements from nVL rock samples from this study. A second mismatch between the two data sets is observed for syenite rocks. Here PetroChron seems to be in an agreement with measurements on rock samples from the Indian Shield, while measurements from this study report lower densities. It is worthwhile to point out that in this study only six measurements have been conducted on Syenite (Fig. 2b), which might not be statistically significant. Furthermore, density measurements on rock samples from the Indian Shield show overall a good agreement with measurements from this study and from PetroChron. Nevertheless, the main density of rocks from the Indian Shield are systematically higher compared to the Antarctic rock samples. This systematic shift might be related to geographical circumstances.

Both comparisons between density and susceptibility measurements on rock samples from nVL to rock samples from the Antarctic Peninsula and Indian Shield indicate that geographical variability can be important (Figs 4 and 5). Therefore, it highlights the need for caution if such measurements are used to validate geophysical models. Geophysical joint inversion models report density and susceptibility relationships as cross plots (Lösing *et al.* 2022; Lowe *et al.* 2023b). However, if the density and susceptibility measurements have not been conducted on the same rock sample, then cross plots of density and susceptibility measurements might be inadequate to validate geophysical inversion models. Mean and standard deviations of density and susceptibility measurements on Australian rocks are simultaneously reported by (Barlow 2004). This data set allows a cross plot comparison between measurements on nVL rock samples, from this study and Australian rock samples. All

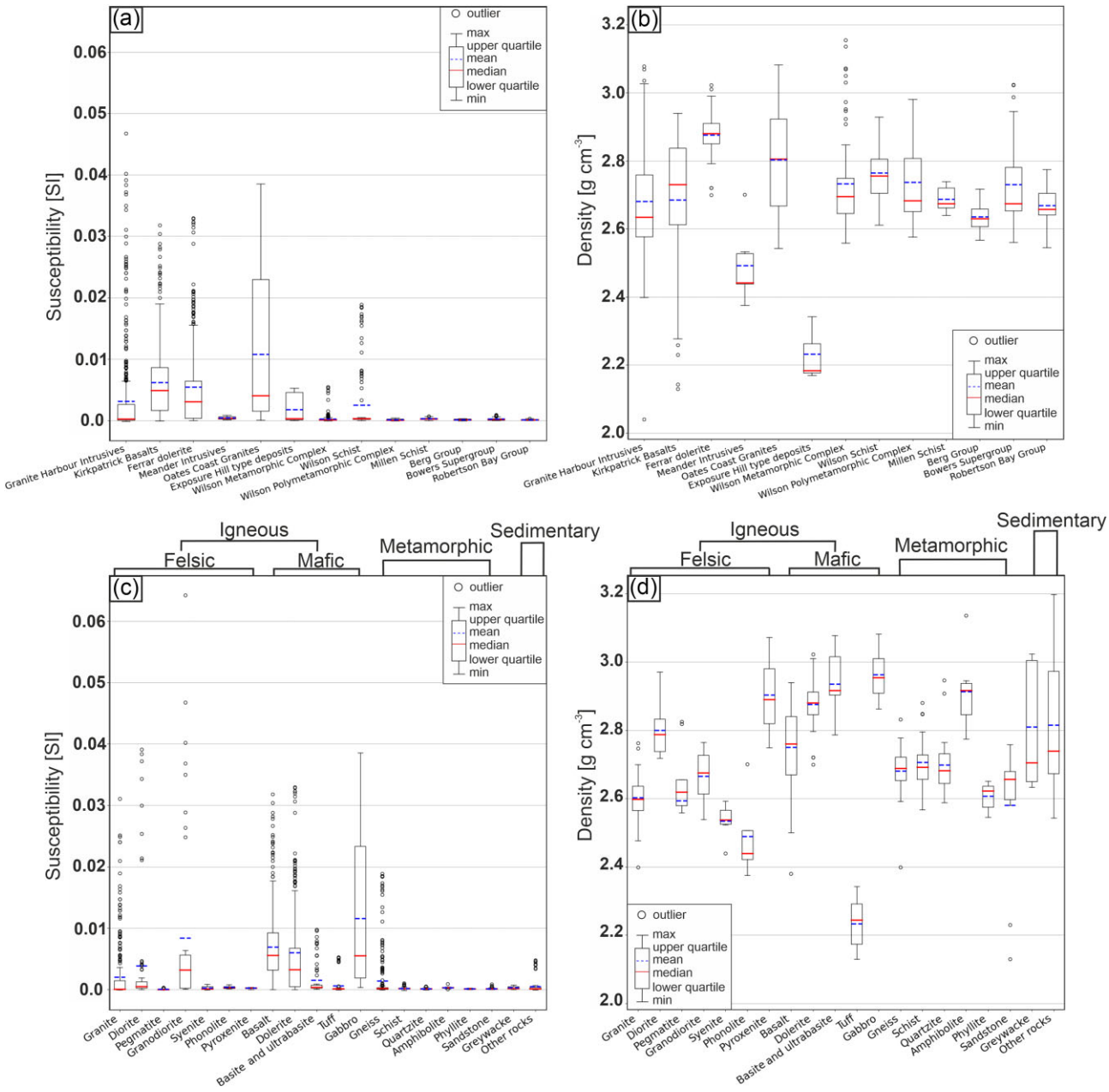

Figure 3. Statistics of measured rock samples. (a) Boxplot of susceptibility measurements sorted by geological formation. (b) Boxplot of density measurements sorted by geological formation. (c) Boxplot of susceptibility measurements sorted by rock type. (d) Boxplot of density meassurments sorted by rock type. Outliers defined as >1.5 times the interquartile ranges.

rock types show a systematic shift to higher mean susceptibility values for Australian rocks (Fig. 6). Similarly, the mean density values are systematically higher for Australian rocks. This shift reinforces the idea of significant geographical variability in petrophysical characteristics in such data sets, especially, when considering the good agreement between density estimation for Antarctic rocks from the PetroChron (Sanchez *et al.* 2021) data set and this study.

Therefore, rock samples geographically closely located should always be given preference before using global rock catalogues or rock samples from neighbouring continents to validate geophysical inversion models. Moreover, this section illustrates that for meaningful comparison it is crucial to have access to the full petrophysical data set (Fig. 5) instead of relying on reported mean values and standard deviations. The internal variability of measurements for a certain rock type is not captured by mean values, while the boxplot comparison (Fig. 5) between density estimation from this study and PetroChron (Sanchez *et al.* 2021) provides a) a higher confidence in the comparison and b) illustrates internal variability for a given rock type.

4 REGIONAL JOINT INVERSION OF MAGNETIC AND GRAVITY DATA

Regional scale VI inversion of magnetic and residual gravity airborne data (Figs S1a and b), which was corrected for gravity contribution from the mantle and below using the (Pappa *et al.* 2019b)

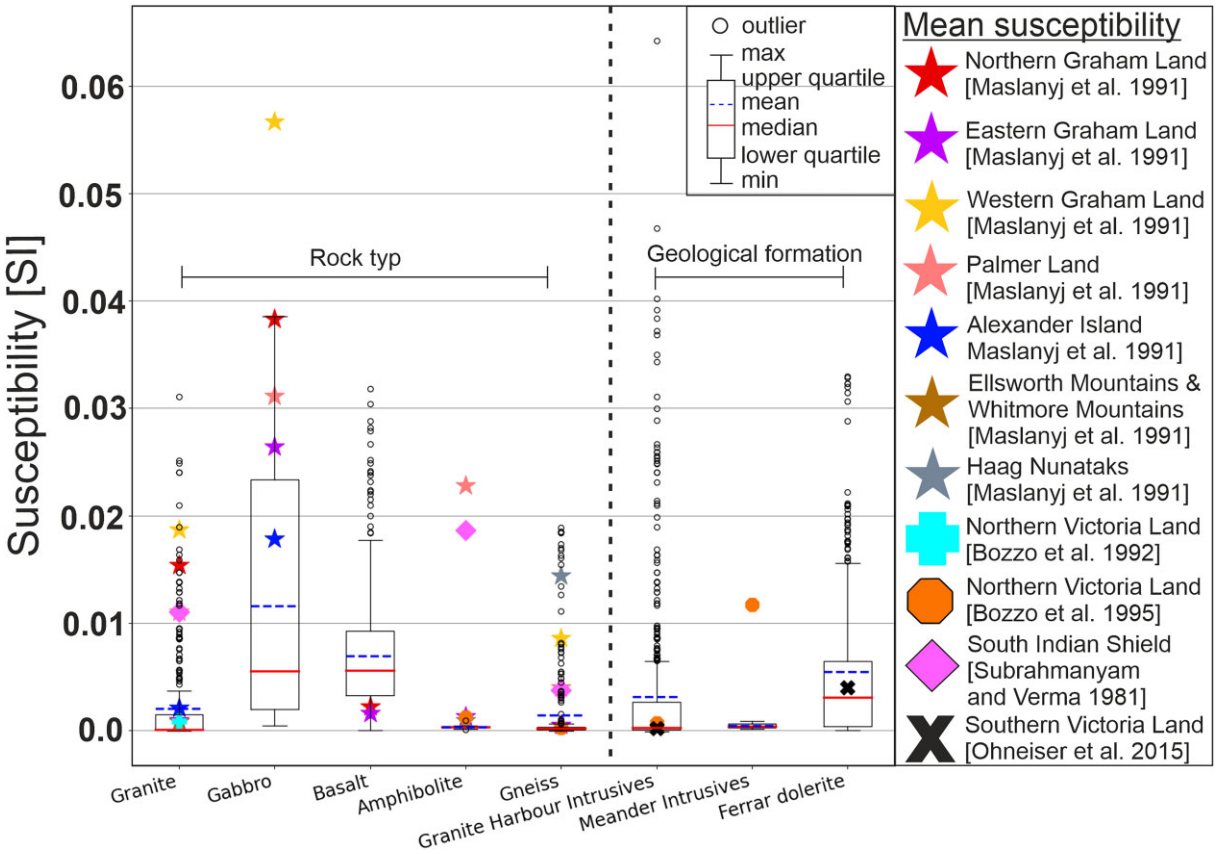

Figure 4. Susceptibility measurements compared to literature values. Susceptibility measurements from this study presented as boxplots. Susceptibility mean measurements on Antarctic rocks displayed as stars (Maslanyj *et al.* 1991), cross (Bozzo *et al.* 1992), octagon (Bozzo *et al.* 1995) and x (Ohneiser *et al.* 2015). Mean susceptibility measurements on rocks from the Indian shield as Rhombus (Subrahmanyam & Verma 1981).

model with a cell size of 7.5 km in nVL and the WSB was carried out and previously described in (Lowe *et al.* 2023b). We used geological classification polygons provided by GeoMap (Cox *et al.* 2023a) to sample the susceptibility and density values at a depth slice of 2 km below sea level (Figs 7a and b) from the inversion model at the locations of specific outcropping rock types. The depth of 2 km was chosen, so that the density and susceptibility values sampled lie within the crust rather than in the domain of the ice sheet, where the inversion cells were set to 0 kg m^{-3} and 0 SI and excluded from the inversion, but also shallow enough that those cells likely correspond to geological classification from GeoMap (Cox *et al.* 2023a) at the surface.

Here we sample the GHI complex (Fig. 8a) at a depth slice of 2 km below sea level and plot the petrological relationship between susceptibility and density as red dots (Fig. 8b) together with laboratory susceptibility (mean susceptibility of eight repeat measurements) and density measurements on GHI complex rock samples as blue dots (Fig. 8b). The inverted susceptibilities are relative values. Therefore, we have shifted the inverted values by 0.008 SI. The value, by which the inverted susceptibilities were shifted was chosen so that the inverted low susceptibility cluster plots around the 0 value and therefore resembles the range of measured susceptibilities more closely. Most of the measured and inverted susceptibilities are low values with occasional outliers. The amplitude range of outliers from the measured rock samples and the inverted values approximately match one another. The points with error bars marked in (Fig. 8b) represent the means of measured and inverted values, while the error bars represent the standard deviations of the respective data sets. The inverted relative density values were shifted to absolute values by adding the background density value of 2670 kg m^{-3}. Measured densities of the GHI complex samples show a larger range than recovered by the VI inversion, but the measured and inverted mean values are located close to one other. However, the density range of the inversion is much narrower compared to the measured density range and does not reproduce the measured high densities above 2900 kg m^{-3} (Fig. 8b).

Subdividing the rock samples from the GHI complex into rock types reveals some lithologies which are poorly fitted and some that are better fitted by the inversion (Fig. 8d). Measured rock types that fall in the inversion density range are granites, granodiorites, gneiss and diorites, while denser rock types that are not well represented by the inversion include hornblendite, ultrabasites and gabbros. The poor representation of the denser rock types by the inversion can be explained by considering the 7.5 km cell size used in this regional inversion. A cell in the inversion mesh represents an average density and susceptibility value of all rock types present in the volume of the cell. In order to reproduce a cell with a density of 3200 kg m^{-3} representing densities of hornblendite, the hornblendite needs to fill the full volume of a 7.5 km by 7.5 km lateral cell. However, high density lithologies are not dominant in the continental crust. Furthermore, hornblendite rocks have densities that are typically associated with density values commonly found in the mantle. The lesson here is that cells of the size used in a regional scale inversion cannot reproduce local small scale geological variation. A regional inversion represents rather large-scale crustal variations and can only reproduce the density/susceptibility of the dominant crustal

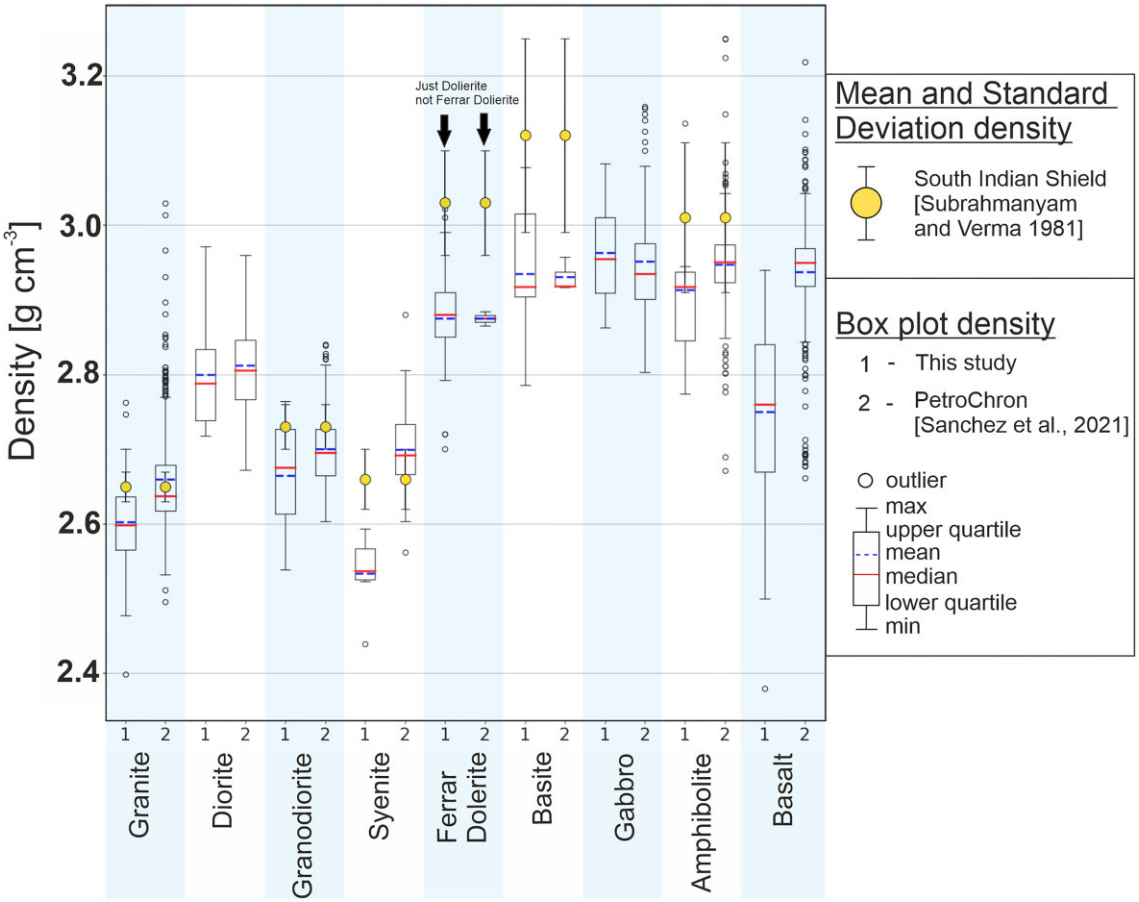

Figure 5. Density measurements from this study compared to literature values. Density estimation from this study and PetroChron (Sanchez *et al.* 2021) displayed as box plots. Mean density estimation on rock samples from Indian Shield (Subrahmanyam & Verma 1981) are displayed as yellow dots. The displayed errors bars illustrate the reported standard deviation.

rocks (average value of all rocks within a given cell). Furthermore, fine scale geological features are often limited to finite depth intervals. For example, individual outcropping sills usually do not exceed thicknesses of ∼200 and 900 m for the Ferrar and the KPB, respectively (Elliot & Fleming 2008; Elliot & Fleming 2018). A regional inversion with vertical cell size of 1 km (reasonable representation of airborne data with 10 km flight line spacing) is unable to resolve exact vertical dimension of such features and will overestimate the thickness. To resolve features like the FD with a 200 m vertical extent, higher resolution airborne data is required.

5 HIGH RESOLUTION LOCAL MAGNETIC-ONLY INVERSION

Magnetic-only inversion is applied to a local helicopter high-resolution magnetic survey of the Mesa Range in nVL, East Antarctica (Fig. 9a). The survey was conducted by the BGR in January 2010 (Damaske *et al.* 2014) with a flight line spacing of 500 m and was flown in draped mode with a ground clearance of about 500 m. The aim of the survey was to determine if prominent circular magnetic anomalies visible in earlier magnetic surveys with wider line spacing are the signals of a feeder dyke complex. Joint inversion is not carried out because only long wavelength airborne gravity data exists in the target area based on three flight lines (Jordan *et al.* 2013), which does not contain comparable short wavelength content to the magnetic data set. Jointly inverting potential field data with a strong discrepancy in wavelength content does not produce meaningful results.

The topography of the target area includes flat-topped mesas as well as deep valleys covered by the overriding Rennick and Aeronaut glaciers (Damaske *et al.* 2014). GeoMap (Cox *et al.* 2023a) shows three dominant geological formations present in the target area, which are KPB, confined to the Mesa topography, FD and GHI complex (Figs 9b and c). The magnetic forward calculated response (Fig. 9b) of the 3-D inverted susceptibility model and the observed magnetic field (Fig. 9a) match closely (Fig. 9c). The mean misfit between the observed and inverted magnetic field is 0.9 nT with a standard deviation of 12 nT. The maximum misfit is 551 nT and the minimum missfit is −130 nT. Areas of significant misfits are limited to a region where the magnetic field rapidly increases locally from ±200 nT to over 1000 nT, in the area of the Mesa Range topography. The misfit arises from a combination of inversion resolution (250 m cell size) and because the inversion favours smooth models compared to steep gradients in the observed magnetic field. The 3-D inversion shows that the dominant magnetic bodies are limited to the volcanic topographic features consisting of KPB. Our inversion indicates these basalts are restricted to high topography and are unlikely to reach depths below sea level, giving a maximum thickness of 2 km, but probably less (Figs 9d and e).

The strong susceptibility signals caused by KPB overlaying the Beacon sediments and crustal basement appear to spread into the underlying crustal basement and the Beacon sediment deposits

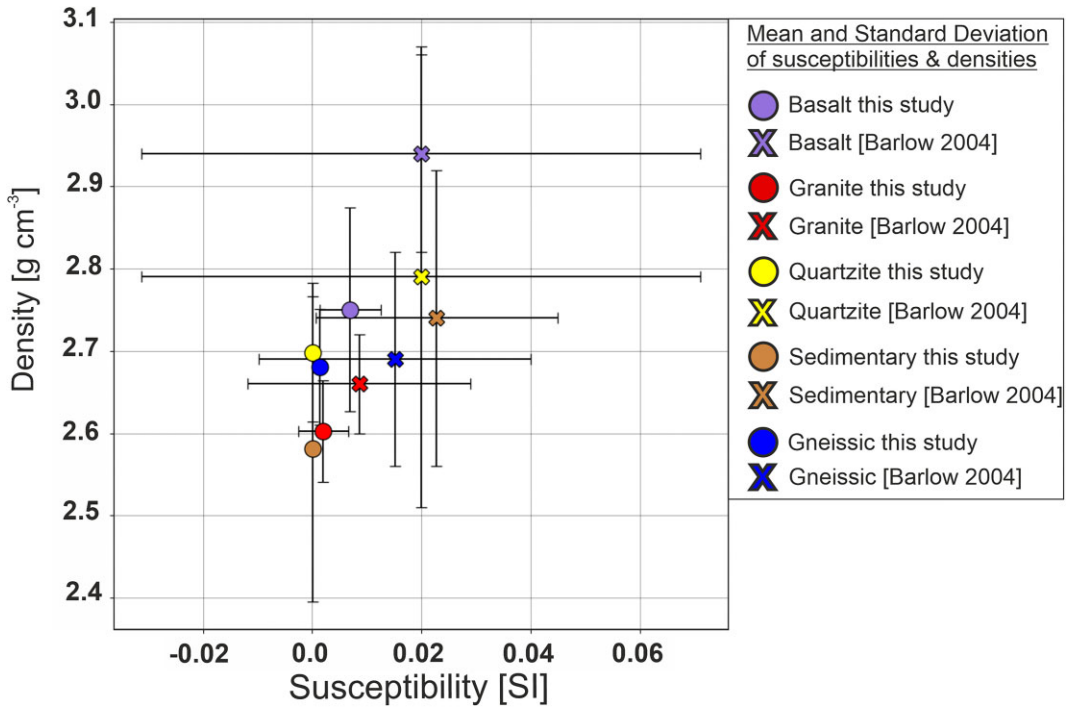

Figure 6. Density and susceptibility cross plot. Measurements from this study are plotted as circles. Density and susceptibility of rock samples from Australia (Barlow 2004) are displayed as diagonal crosses. Standard deviations for both data sets are displayed as error bars.

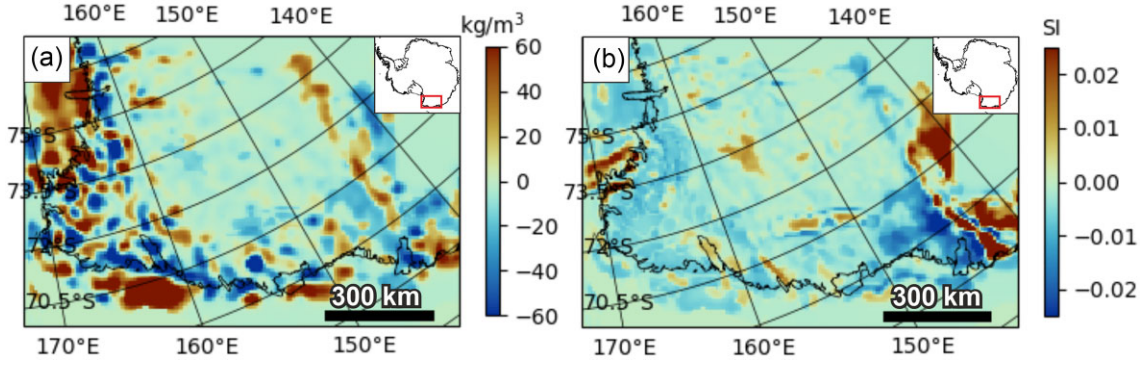

Figure 7. Inverted density and susceptiblity distribution of regional scale joint inversion model (Lowe *et al.* 2023a). (a) Inverted relative density at 2 km depth. (b) inverted relative susceptibility at 2 km depth. Inverted crustal density and susceptibility distribution from regional scale VI inversion with a horizontal cell resolution of 7.5 km (Lowe *et al.* 2023b).

(Figs 9d and e). Inverting jointly with gravity data of matching resolution could help to focus the source bodies and reduce the vertical smearing of the anomalies. This spreading effect lets the susceptibility source bodies appear to reach thicknesses of 2 km while the source body with the highest susceptibilities values are limited to thicknesses of less than 1 km. Geological evidence exists that the thickness of KPB is limited to a maximum of 900 m in nVL (Elliot & Fleming 2008; Elliot & Fleming 2018).

We do not see evidence for a feeder dyke complex in our high-resolution 3-D susceptibility inversion, due to the absence of deeper magnetic bodies in the Mesa Range area. This result is in line with previous 2-D modelling from (Damaske *et al.* 2014) who did not find feeder dykes for the basalt sheets either but identified circular-shaped anomalies visible in an earlier aerogeophysical survey as artefacts due to wider line spacings. Furthermore, both results are in line with the absence of geological evidence for feeder dykes, dyke swarms, or vents in nVL. The pathways of magma emplacement are currently unknown (e.g. Elliot & Fleming 2018; Elliot *et al.* 2021).

A secondary prominent magnetic signature in the area is visible with a lower magnitude (Fig. 9d). This signature also correlates closely with the topography but does not coincide with the highest topographic peaks. Those magnetic bodies match with the areas in which there are outcrops classified as FD (Figs 10b and c) based on GeoMap (Cox *et al.* 2023a). These dolerite sills intruded into the surrounding sedimentary Beacon Supergroup (Ferraccioli *et al.* 2009). FD and KPB can be separated based on the inverted susceptibility intensity and based on the correlation with topographic highs displayed in cross section view (Fig. 9d).

We can also use the inverted susceptibility distribution to separate the three dominant geological units namely KPB, FD and GHI Complex. Fig. 10(a) shows the inverted susceptibility distribution sampled for each geological unit in the Mesa Range at a depth of

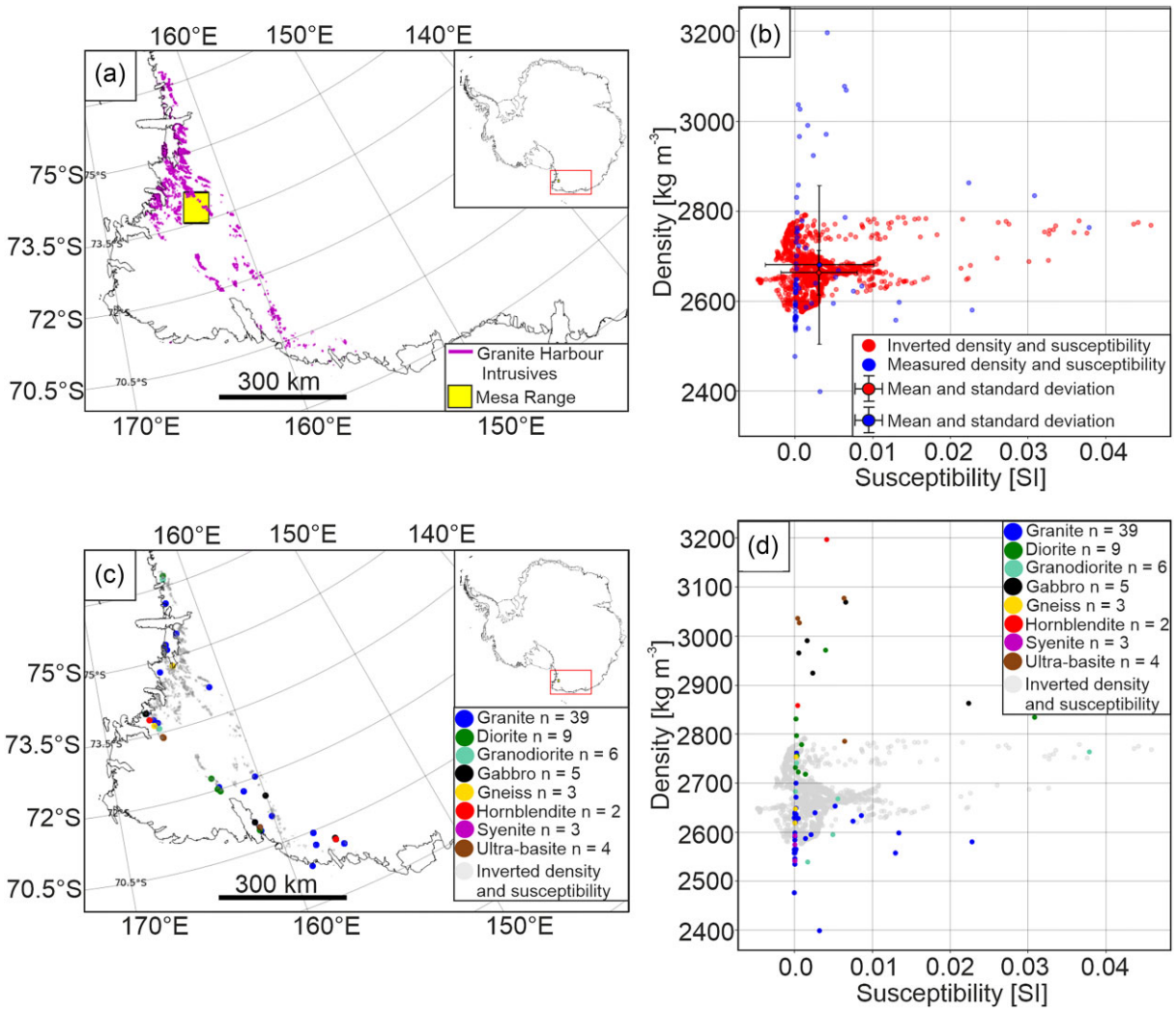

Figure 8. (a) GHI complex polygons from GeoMap (Cox *et al.* 2023a). (b) Inverted (red) and measured (blue) susceptibility and density crossplot for GHI complex (here the susceptibility values describe the mean value of eight repeat measurements). Datapoints with error bars represent the mean datapoints of inverted and measured data sets, while the error bars represent the standard deviation of each data set. (c) Location of rock samples within the GHI complex coloured by rock type superimposed on GHI complex polygon from GeoMap (Cox *et al.* 2023a). (d) Measured susceptibility and density crossplot for the GHI complex, coloured by rock type and superimposed on GHI complex inverted sucesptibility and density crossplot (grey).

1.8 km above sea level using the GeoMap (Cox *et al.* 2023a). The rock classification polygons are shown in Fig. 10(b). The 1.8 km depth slice was chosen so that near surface susceptibility values are extracted, which relate to surface geological classifications based on GeoMap (Cox *et al.* 2023a) and the main units are well represented in the model (within the crustal domain). In addition to the histogram of the inverted susceptibility for each rock type, kernel density estimates (KDE) are plotted to illustrate the bulk susceptibility distribution for each rock type. The area beneath each KDE curve is 1 and therefore illustrates that KBP has a larger distribution compared to FD and GHI which are confined to finite ranges Fig. 10(a). The large range of inverted KPB susceptibilities partly overlap with the inverted susceptibility range of the FD (Fig. 10a). However, the inverted susceptibilities from the KPB unit extend to higher values (0.019–0.08 SI), while the inverted susceptibilities of the FD are concentrated at medium values. The medium susceptibility range is populated by all three geological units, while the low susceptibility range is dominated by FD and GHI Complex. The inverted susceptibilities are in line with laboratory measurements on rock samples from nVL (Figs 2 and 3).

Based on the susceptibility distribution we filter the inversion model for two susceptibility ranges which we attribute to KPB and FD (Fig. 10a). Susceptibility values above 0.019 SI match very well with the KPB locations from GeoMap (Cox *et al.* 2023a; Fig. 10c) and the laboratory measured susceptibility (Fig. 10d). The intermediate ranges correspond to the dominant FD susceptibility distribution from 0.0047 to 0.018 and match well with the locations of FD from GeoMap (Cox *et al.* 2023a, Fig. 10c). Even though FD and GHI complex overlap strongly in the low susceptibility range, the chosen susceptibility range for FD shows a good fit with classified rock outcrops from GeoMap (Cox *et al.* 2023a) and a sharp boundary between FD and GHI complex is observed in the inversion results (dotted yellow lines in Fig. 10c). From the geophysical inversion model, based on the FD susceptibility range, we can identify locations with high likelihood of FD occurrence where geological mapping is missing, marked as ‘F’ in (Figs 10b and c).

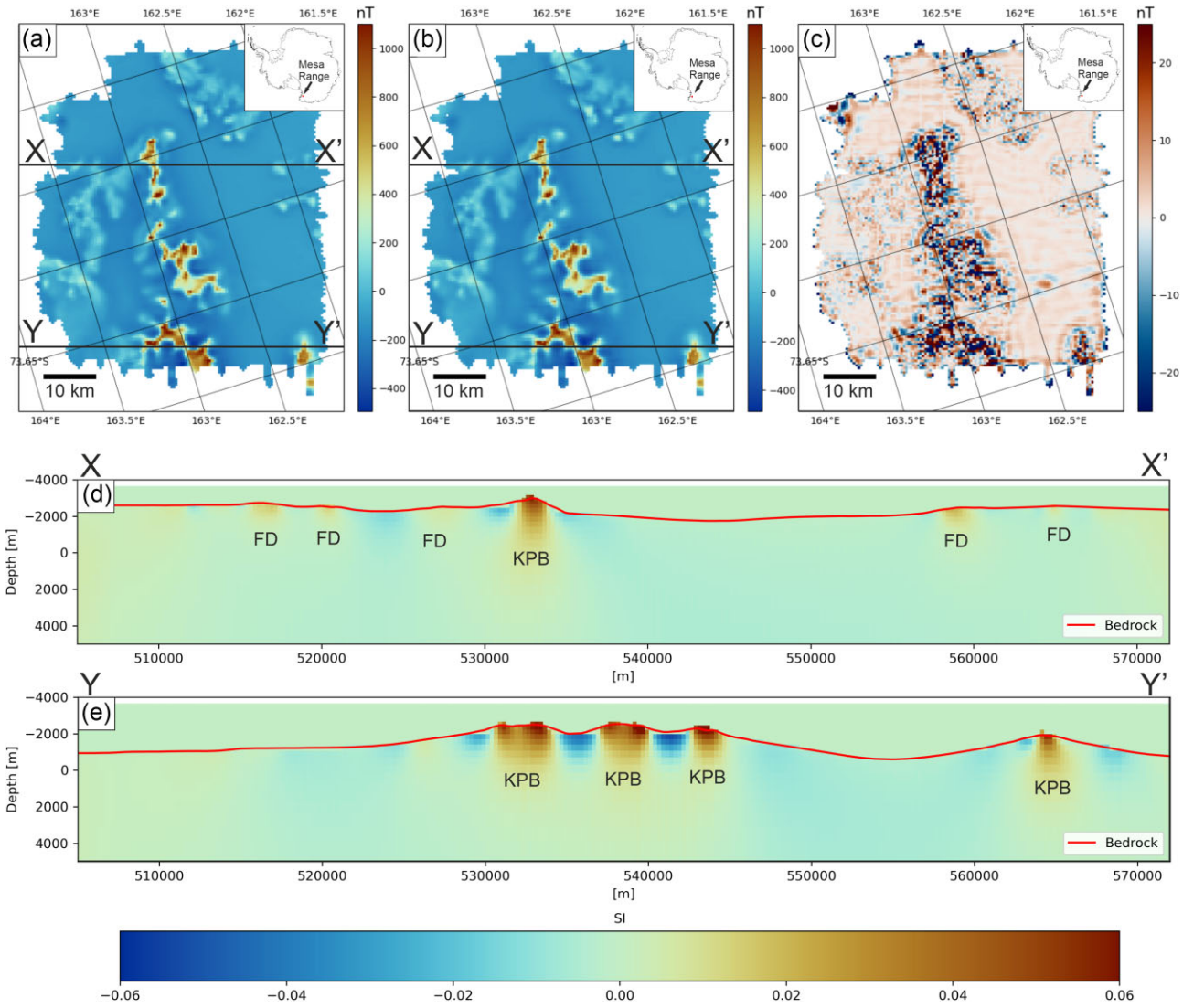

Figure 9. Magnetic data and inversion results over the Mesa Range. (a) Observed magnetic field. (b) Inverted magnetic field. (c) Misfit between (a) and (b). (d) and (e) Cross-section through inverted suscepitibility distribution along profile lines indicated in (a) and (b).

Linking susceptibility values from Antarctic rock samples with forward or inverse models is rare in the literature, due to the limited number of measurements on Antarctic rock samples, but such efforts have been made before (e.g. Maslanyj *et al.* 1991; Bozzo *et al.* 1992; Bozzo *et al.* 1995). Histogram distributions of measured and inverted susceptibilities for the Mesa Range highlight that the susceptibility ranges are well represented (Fig. 11). However, although end-member values are similar, the peak accumulations of measured and inverted susceptibilities for FD are offset (Fig. 11). The broad range of susceptibilities for the KPB is also recovered by measurements, but it is apparent that higher susceptibilities are required by the inversion model for the KPD to fit the observed magnetic field than were recovered from the rock sample measurements (Fig. 11). In both cases, it is worth remembering that the sample size from the inversion is significantly larger than the rock sample size presented in this study.

Density measurements on the same rock samples as the susceptibility measurements indicated that FD (average 2877 kg m^{-3}), KPB (average 2747 kg m^{-3}) and GHI complex (average 2603 kg m^{-3}) can be distinguished by density. Discrimination of rock units like KPB, FD and GHI complex could be significantly improved by using density inversions and measurements (Fig. 10d). However, as discussed before, gravity measurements with similar resolution to that of the Mesa Range magnetic survey are currently missing in Antarctica. Regardless, the laboratory density measurements indicate the high potential of using joint density and susceptibility inversion of ultra-high-resolution gravity and magnetic data to reveal subglacial geology in the future.

It is apparent from the laboratory petrological measurements and the inversion models that the geological units have high internal variability. Therefore, there is a strong incentive for crustal Antarctic models to use the sparse existing rock samples/rock outcrop data to validate geophysical models with local geological information rather relying on rock property catalogues consisting of global or Australian rock samples (Section 3.2), and to solve or incorporate the internal variability into geophysical crustal models.

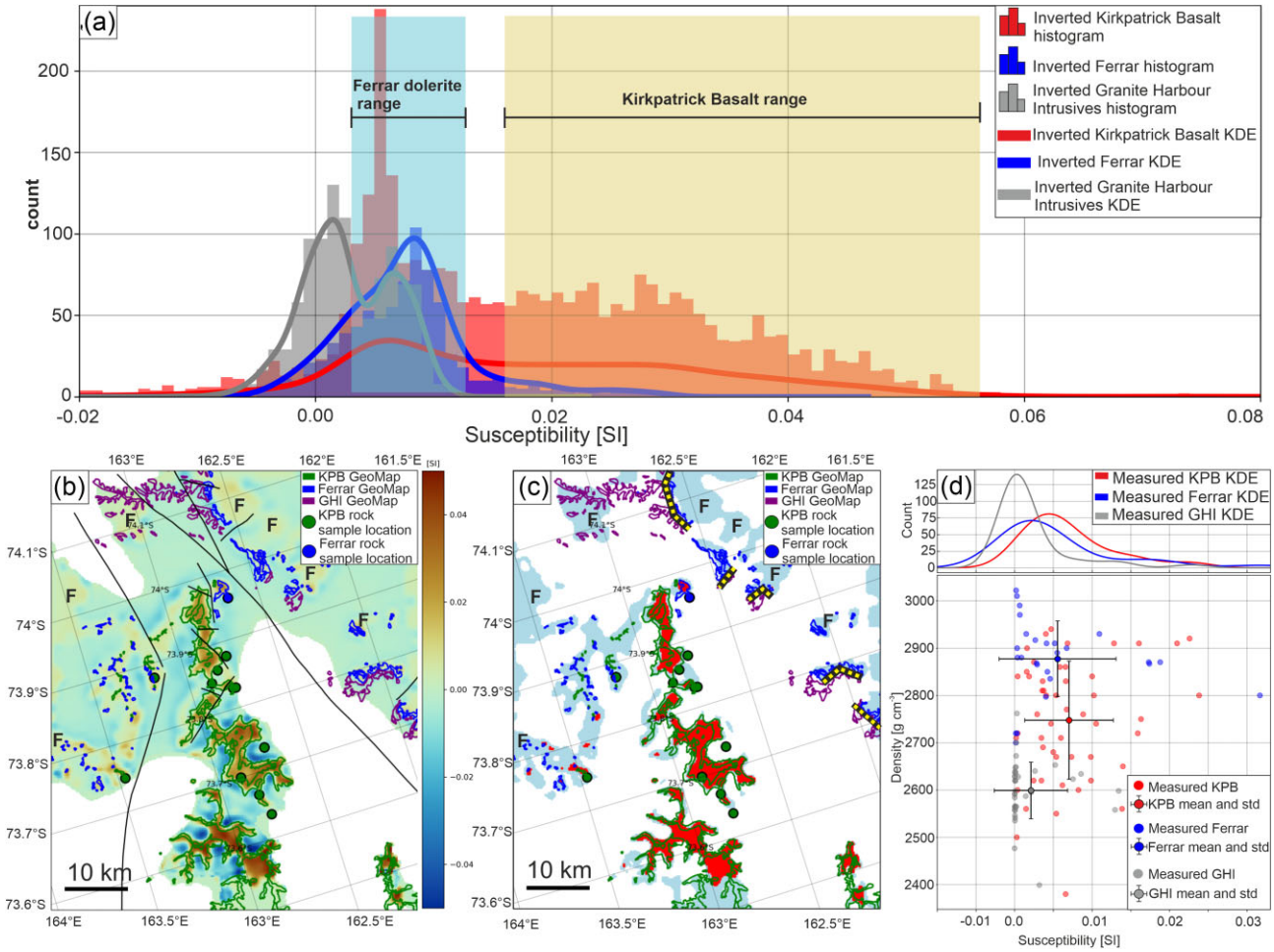

Figure 10 (a) Inverted susceptibility distribution of geological units sampled against GeoMap (Cox *et al.* 2023b) polygons at a depth of 1.8 km above the sea level. Area beneath each kernel density estimation (KDE) curve adds up to 1. (b) GeoMap (Cox *et al.* 2023a) classification superimposed on susceptibility depth slice from high-resolution magnetic data inversion at 1.8 km above sea level. Additionally, locations of rock samples are marked. Areas where the depth slice is above the bedrock appear white. Black lines indicate faults after (Cox *et al.* 2023b) (c) location plot of susceptibility values wihin predefined susceptibility ranges for each lithology shown in a. Yellow dotted lines are interpreted lithological boundaries between Ferrar and GHI complex. 'F' indicates region of high probability of FD rocks buried beneath the ice. (d) Density susceptibility crossplot of measured rock types present in the Mesa Range. Location of the Mesa Range shown in Fig. 1.

6 CONCLUSION AND FUTURE WORK

We demonstrated that our new petrological measurements on 320 rock samples can help interpret geophysical models on both regional and local scales in nVL. VI inversion can reproduce the susceptibility distribution on a regional scale, but the inverted density distribution has the caveat that only the average density value is reproduced for each cell, meaning only the dominant lithology (average physical properties) can be recovered. Additionally, comparison between this petrophysical rock catalogue and literature values shows that significant geographical variability can be observed. This highlights that rock samples geographically close to the study area should always be prioritised before using petrophysical catalogues including global rock samples. If more general petrophysical catalogues are used to validate geophysical models, caution is required to not overinterpret results since local variability might not be reflected.

Additionally, we demonstrate that high resolution 3-D susceptibility inversion on a local scale with a mesh cell size of 250 m is capable of identifying KPB and constraining the depth extent of those magnetic bodies to a thickness of less than 2 km. KPB and FD can be reliably discriminated by the susceptibility inversion. The predicted location based on susceptibility ranges matches well with geological classification from GeoMap (Cox *et al.* 2023a) and allows us to predict locations with a high probability of FD in ice-covered areas and where geological mapping is missing.

Furthermore, no evidence is visible in the high resolution 3-D magnetic inversion for the presence of feeder dykes in the Mesa Range in nVL, due to the absence of deeper magnetic bodies as previously concluded by magnetic anomaly map interpretation combined with 2-D profile modelling by (Damaske *et al.* 2014).

Separating the FD and the GHI complex using inverted susceptibility is more challenging due to their overlapping susceptibility range in the low value domain. Density measurements show that all three dominating geological units present in the Mesa Range (KPB, FD and GHI complex) show distinct density clusters. FD and GHI complex could be separated by inverted densities and the uncertainty of the discrimination between KPB, and FD would be further reduced by utilising inverted densities. However, this would require high resolution gravity surveys (with less than 1 km flight line spacing and high-resolution along line) that can resolve suitable

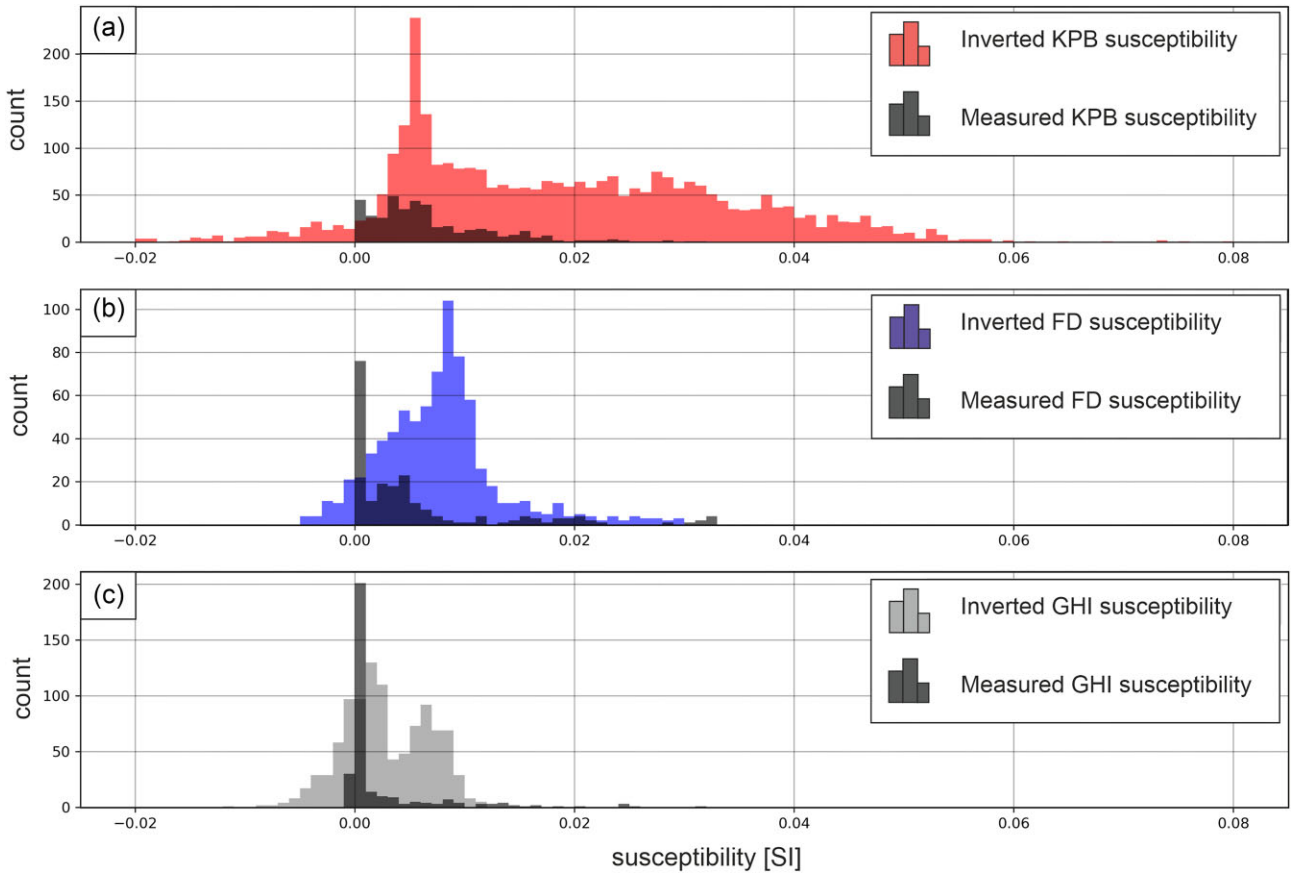

Figure 11. Comparison of measured and inverted susceptibility for (a) KPB, (b) FD and (c) GHI complex.

short wavelength anomalies. Such surveys are currently missing in Antarctica. This study highlights the high potential of joint inversion of high-resolution gravity and magnetic data in combination with local petrological catalogues to reveal fine scale subglacial geological structures. It also shows the potential of this approach to relate geological and geophysical models on a local scale in regions where a high density or susceptibility contrast is expected to occur due to strong lithological changes. Furthermore, this study illustrates how high-resolution airborne gravity surveys would enable more reliable discrimination of different rock types and provides motivation to consider ways to incorporate internal variability of density and susceptibility of geological units in geophysical crustal forward or inverse models.

AUTHOR CONTRIBUTIONS

Maximilian Lowe (Conceptualization, Data curation, Formal analysis, Investigation, Methodology, Software, Validation, Visualization, Writing – original draft, Writing – review & editing); Tom Jordan (Conceptualization, Formal analysis, Funding acquisition, Investigation, Methodology, Project administration, Supervision, Validation, Visualization, Writing – review & editing); Jörg Ebbing (Conceptualization, Data curation, Formal analysis, Investigation, Methodology, Supervision, Validation, Visualization, Writing – review & editing); Nikola Koglin (Data curation, Formal analysis, Investigation, Validation, Writing – review & editing); Antonia Ruppel (Data curation, Formal analysis, Investigation, Validation, Writing – review & editing); Max Moorkamp (Conceptualization, Formal analysis, Investigation, Methodology, Software, Validation, Visualization, Writing – review & editing); Andreas Läufer (Formal analysis, Investigation, Validation, Visualization, Writing – review & editing); Chris Green (Conceptualization, Formal analysis, Investigation, Methodology, Supervision, Visualization, Writing – review & editing); Jonas Liebsch (Data curation, Formal analysis, Writing – review & editing); Mikhail Ginga (Data curation, Formal analysis, Writing – review & editing) and Robert Larter (Conceptualization, Formal analysis, Funding acquisition, Investigation, Methodology, Project administration, Supervision, Validation, Visualization, Writing – review & editing).

ACKNOWLEDGMENTS

Funding for this research was provided by NERC through a SENSE CDT studentship (NE/T00939X/1). ML acknowledges additional funding through the Gray-Milne Travel Bursary provided by the British Geophysical Association. We thank Graeme Eagles, the anonymous reviewer, and the Editors for their thorough review and constructive comments, which helped to improve the paper. The authors thank the developers of open scientific software products which were utilized in this study: JIF3D developed by Max Moorkamp is available under a GNU General Public License (v3) via subversion at https://svn.code.sf.net/p/jif3d/jif3dsvn/trunk/jif3D; NumPy (Harris *et al.* 2020); Matplotlib (Hunter 2007); Pandas (McKinney 2010); Geopandas (Jordahl *et al.* 2020); Cmcrameri (Crameri 2023); Cartopy (Elson *et al.* 2022); Shapley (Gillies *et al.* 2022); SciPy (Virtanen *et al.* 2020) and Jupyter notebook (Kluyver *et al.* 2016).

SUPPORTING INFORMATION

Supplementary data are available at *GJIRAS* online.

Figure S1. (a) Residual gravity map, which was used for the joint inversion on a regional scale. The residual gravity field is obtained by subtracting the gravity response from the lithospheric model of (Pappa *et al.* 2019b) from Bouguer Anomaly data from (Reitmayr *et al.* 2003; Scheinert *et al.* 2016; Zanutta *et al.* 2018). Subsequent the mean value of the residual field was subtracted. (b) Magnetic anomaly grid from ADMAP-2 (Golynsky *et al.* 2018). Both the residual and gravity field have a gridspacing of 10 km and a station height of 10 km. Black lines indicate faults after GeoMap (Cox *et al*. 2023a, b).

Figure S2. (a) Moho depth map derived from Satellite gravity measurements (Pappa *et al.* 2019a). (b) Curie point depths estimated (Lowe *et al*. 2023a, b) based on kriging interpolation. Were Curie Point depths exceed Moho depth, the Moho depth value is used as Curie Point depth. Black lines indicate faults after GeoMap (Cox *et al*. 2023a, b).

Figure S3. Bedrock topography of the Transantarctic Mountains and Wilkes Subglacial Basin from the Bedmachine model version 3 [Morlighem *et al.* 2020]. EB: Eastern Basin; CB: Central Basin; WB: Western Basin; MSZ: Mertz shear zone. Black lines mark ice grounding lines, ice shelf extents, and faults from GeoMap (Cox *et al*. 2023a, b).

Figure S4. Local inversion model setup in the Mesa Range region. (a) Bedrock topography from BedMachine (Morlighem *et al.* 2020). (b) Curie Point Depths (CPD) from (Lowe *et al*. 2023a, b). (c) cross plot through inversion model set up. Cells between bedrock and CPD are allowed to vary during the inversion, marked as yellow cells. Purple coloured cells represent air and cells below the CPD, which are not allowed to vary during the inversion. Cells increase vertically with depth and horizontal within the padding area.

Figure S5. Inverted susceptibility distribution based on different inversion runs with varying regularisation parameters. Profile location given in (Fig. S7). Regularisation values influences any inversion. In this study (main text) we have chosen a very low regularisation value of 10. With increasing regularisation parameter, the misfit between observed and inverted field increases. The inversion, with a regularisation value of 100 produces a susceptibility distribution, which is in the same susceptibility range as the inversion with a regularisation of 10. However, this inversion recovers deeper structures, which are inconsistent with geological information and the standard deviation is slightly larger. Regularisation parameter values above 1000 do not reproduce the amplitude of the observed magnetic field anymore.

Figure S6. Inverted susceptibility distribution based on different inversion runs with varying regularisation parameters. Profile location given in (Fig. S7). Regularisation values influences any inversion. In this study (main text) we have chosen a very low regularisation value of 10. With increasing regularisation parameter, the misfit between observed and inverted field increases. The inversion, with a regularisation value of 100 produces a susceptibility distribution, which is in the same susceptibility range as the inversion with a regularisation of 10. However, this inversion recovers deeper structures, which are inconsistent with geological information and the standard deviation is slightly larger. Regularisation parameter values above 1000 don't reproduce the amplitude of the observed magnetic field anymore.

Figure S7. Comparison of observed magnetic data (left-hand panel) to the inverted magnetic field (middle panel). Difference between both fields is given on the right-hand panel. Left-hand and middle panel provide location of the profiles shown in (Figs S5 and S6).

Please note: Oxford University Press is not responsible for the content or functionality of any supporting materials supplied by the authors. Any queries (other than missing material) should be directed to the corresponding author for the paper.

DATA AVAILABILITY

Petrological catalogue of Susceptibility and density on rock samples from northern Victoria Land (Lowe *et al.* 2024b) is available through the UK polar data centre https://doi.org/10.5285/9ac70954-80aa-45af-b70f-e4e45efa8293.

Inverted susceptibility distribution model in the Mesa Range region, Antarctica based on high resolution magnetic data (Lowe *et al.* 2024a) is available through the UK polar Data centre at: https://doi.org/10.5285/ff3798b8-146f-42c2-870e-64c738970350.

Python code including preparation and illustration of the local inversion model as well as the python code used for the presented interpretation are presented as jupyter notebooks and available through zenodo at https://doi.org/10.5281/zenodo.10822142

CPD data set (Lowe *et al.* 2022) available at https://doi.org/10.5285/B8DCBAA9-3AC0-42BD-95A5-6B5961CBCB7E.

Regional density and susceptibility model based on VI joint inversion (Lowe *et al.* 2023a) available at https://doi.org/10.5285/5e1424e7-124d-4cc3-ba06-b2285c0b458c.

Bedrock topography from 'BedMachine Antarctica version 3″ (Morlighem *et al.* 2022) is freely available at https://nsidc.org/data/nsidc-0756/versions/3.

GeoMap (Cox *et al.* 2023b) is available at https://doi.org/10.1594/PANGAEA.951482.

REFERENCES

Aitken, A.R.A. *et al.* 2014. The subglacial geology of Wilkes Land, East Antarctica, *Geophys. Res. Lett.,* **41,** 2390–2400.

Barlow, M., 2004. Density and susceptibility characterization of major rock units and rock types of Mount Isa Inlier i1 & i2 projects pmd∗CRC Internal report, eCatId: 67942. Commonwealth of Australia (Geoscience Australia), https://ecat.ga.gov.au/geonetwork/srv/api/records/a05f7892-da0b-7506-e044-00144fdd4fa6.

Barrett, P.J. & Froggatt, P.C., 1978. Densities, porosities, and seismic velocities of some rocks from Victoria Land, Antarctica, *N.Z. J. Geol. Geophys.,* **21,** 175–187.

Blakely, R.J., 1996. *Potential Theory in Gravity and Magnetic Applications,* Cambridge Univ. Press.

Bozzo, E., Caneva, G., Capponi, G. & Colla, A., 1995. Magnetic investigations of the junction between Wilson and Bowers terranes (northern Victoria Land, Antarctica), *Antarct. Sci.,* **7,** 149–157.

Bozzo, E., Colla, A. & Meloni, A., 1992. Ground magnetics in North Victoria Land (East Antarctica), in *Recent Progress in Antarctic Earth Science,* pp. 563–569, eds Yoshida, Y., Kaminuma, K. & Shiraishi, K., Terra Scientific Publishing Company.

Cox, S.C. *et al.*, 2023a. A continent-wide detailed geological map data set of Antarctica, *Sci. Data,* **10,** 250.

Cox, S.C. *et al.*, 2023b. The GeoMAP (v.2022-08) continent-wide detailed geological data set of AntarcticaPANGAEA.

Crameri, F., 2023. Scientific colour maps [Software], Zenodo.

Damaske, D., Schreckenberger, B. & Goldmann, F., 2014. A high resolution aeromagnetic survey over the Mesa Range, northern Victoria Land, Antarctica, *Polarforschung,* **84,** 1–13.

Elliot, D.H. & Fleming, T.H., 2008. Physical volcanology and geological relationships of the jurassic Ferrar Large igneous Province, Antarctica, *J. Volc. Geotherm. Res.,* **172,** 20–37.

Elliot, D.H. & Fleming, T.H., 2018. The Ferrar Large Igneous Province: field and geochemical constraints on supra-crustal (high-level) emplacement of the magmatic system, in *Large Igneous Provinces from Gondwana and Adjacent Regions,* pp. 41–58, eds Sensarma, S. & Storey, B.C., Geological Society Special Publication 463, Geological Society of London.

Elliot, D.H., White, J.D.L. & Fleming, T.H., 2021. Chapter 2.1a: Ferrar large igneous province: volcanology, in *Volcanism in Antarctica: 200 Million Years of Subduction, Rifting and Continental Break-up,* eds Smellie, J.L., Panter, K.S. & Geyer, A., Geological Society of London.

Elson, P. *et al.* , 2022. SciTools/cartopy: v0.21.1 [Software], Zenodo.

Ferraccioli, F., Armadillo, E., Jordan, T.A., Bozzo, E. & Corr, H., 2009. Aeromagnetic exploration over the East Antarctic Ice Sheet: a new view of the Wilkes Subglacial Basin, *Tectonophysics,* **478,** 62–77.

Ferraccioli, F., Finn, C.A., Jordan, T.A., Bell, R.E., Anderson, L.M. & Damaske, D., 2011. East Antarctic rifting triggers uplift of the Gamburtsev Mountains, *Nature,* **479,** 388–392.

Ghirotto, A., Armadillo, E., Crispini, L., Zunino, A., Tontini, F.C. & Ferraccioli, F., 2023. The sub-ice structure of Mt. Melbourne volcanic field (Northern Victoria Land, Antarctica) uncovered by high-resolution aeromagnetic data, *J. geophys. Res.,* **128,** e2022JB025687.

Gibson, G.M., Champion, D.C. & Ireland, T.R., 2015. Preservation of a fragmented late Neoproterozoic–earliest cambrian hyper-extended continental-margin sequence in the australian delamerian Orogen, *Geol. Soc., Lond., Spec. Publ.,* **413,** 269–299.

Gillies, S. *et al.*, , 2022. Shapely [Software], Zenodo.

Giordano, G., Lucci, F., Phillips, D., Cozzupoli, D. & Runci, V., 2012. Stratigraphy, geochronology and evolution of the Mt. Melbourne volcanic field (North Victoria Land, Antarctica), *Bull. Volcanol.,* **74,** 1985–2005.

Golynsky, A.V. *et al.*, 2018. New Magnetic anomaly map of the Antarctic, *Geophys. Res. Lett.,* **45,** 6437–6449.

Goodge, J.W., 2020. Geological and tectonic evolution of the Transantarctic Mountains, from ancient craton to recent enigma, *Gondwana Res.,* **80,** 50–122.

Goodge, J.W. & Finn, C.A., 2010. Glimpses of East Antarctica: aeromagnetic and satellite magnetic view from the central Transantarctic Mountains of East Antarctica, *J. geophys. Res.,* **115,** doi:10.1029/2009JB006890.

Haggerty, S.E., 1978. Mineralogical contraints on Curie isotherms in deep crustal magnetic anomalies, *Geophys. Res. Lett.,***5,** 5, 105–108.

Harris, C.R. *et al.*, 2020. Array programming with NumPy, *Nature,* **585,** 357–362.

Hunter, J., 2007. Matplotlib: a 2D graphics environment, *Comput. Sci. Eng.,* **9,** 90–95.

Jordahl, K. *et al.* , 2020. geopandas/geopandas: v0.8.1 [Software], Zenodo.

Jordan, T.A., Ferraccioli, F., Armadillo, E. & Bozzo, E., 2013. Crustal architecture of the Wilkes Subglacial Basin in East Antarctica, as revealed from airborne gravity data, *Tectonophysics,* **585,** 196–206.

Jordan, T.A., Ferraccioli, F. & Forsberg, R., 2022. An embayment in the East Antarctic basement constrains the shape of the Rodinian continental margin, *Commun. Earth Environ.,* **3,** 52, doi:10.1038/s43247-022-00375-z.

Jordan, T.A., Thompson, S., Kulessa, B. & Ferraccioli, F., 2023. Geological sketch map and implications for ice flow of Thwaites Glacier, West Antarctica, from integrated aerogeophysical observations, *Sci. Adv.,* **9,** eadf2639, doi:10.1126/sciadv.adf2639.

Kluyver, T. *et al.*, 2016. Jupyter Notebooks—A publishing format for reproducible computational workflows, in *Positioning and Power in Academic Publishing: Players, Agents and Agendas,* pp. 87–90, IOS Press.

Kyle, P.R., 1990. A. McMurdo Volcanic Group Western Ross Embayment, in *Volcanoes of the Antarctic Plate and Southern Oceans,* Vol. **48,** pp. 18–145, eds LeMasurier, W.E., Thomson, J.W., Baker, P.E., Kyle, P.R., Rowley, P.D., Smellie, J.L. & Verwoerd, W.J., Antarctic Research Series, AGU.

Kyle, P.R. & Cole, J.W., 1974. Structural control of volcanism in the McMurdo Volcanic Group, Antarctica, *Bull. Volcanol.,* **38,** 16–25.

Läufer, A., Lisker, F. & Phillips, G., 2011. Late Ross-orogenic deformation of basement rocks in the northern Deep Freeze Range, Victoria Land, Antarctica: the Lichen Hills shear zone, *Polarforschung, Bremerhaven, Alfred Wegener Institute for Polar and Marine Research & German Society of Polar Research,* **80**(2), 60–70.

Lösing, M., Moorkamp, M. & Ebbing, J., 2022. Joint inversion based on variation of information—a crustal model of Wilkes Land, East Antarctica, *Geophys. J. Int.,***232,** 162–175,

Lowe, M., Mather, B., Green, C., Jordan, T.A., Ebbing, J. & Larter, R., 2022. *Curie Depth Points and Geothermal Heat Flow Estimates from Spectral Analysis of Magnetic Data in the Transantarctic Mountains and Wilkes Subglacial Basin Region, (Version 1.0) [Data set],* NERC EDS UK Polar Data Centre.

Lowe, M., Jordan, T., Moorkamp, M., Ebbing, J., Green, C., Lösing, M. & Larter, R., 2023a. *3D density and Susceptibility Distribution of the Wilkes Subglacial Basin and Transantarctic Mountains in East Antarctica, (Version 1.0) [Data set],* NERC EDS UK Polar Data Centre, .

Lowe, M., Jordan, T.A., Moorkamp, M., Ebbing, J., Green, C., Lösing, M. & Larter, R., 2023b. *The 3D Crustal Structure of the Wilkes Subglacial Basin, East Antarctica, Based on Joint Inversion of Gravity and Magnetic Data Using Variation of Information,* Authorea, Inc.

Lowe, M., Mather, B., Green, C., Jordan, T.A., Ebbing, J. & Larter, R., 2023c. Anomalously high heat flow regions beneath the Transantarctic Mountains and Wilkes Subglacial Basin in East Antarctica inferred from curie depth, *J. geophys. Res.,* **128,** e2022JB025423.

Lowe, M. *et al.*, 2024a. *3D susceptibility Distribution Model Derived from 2010 BGR Magnetic Survey of the Mesa Range in northern Victoria Land, East Antarctica (Version 1.0) [Data set]*. NERC EDS UK Polar Data Centre.

Lowe, M. *et al.*, 2024b. *Density and Susceptibility Catalogue of 320 Rock Samples from northern Victoria Land, East Antarctica (Version 1.0) [Data set]*. NERC EDS UK Polar Data Centre.

Maslanyj, M.P., Garrett, S.W., Johnson, A.C., Renner, A.C. & Smith, A.M., 1991. *Aeromagnetic Anomaly Map of West Antarctica (Weddell Sea sector), Scale 1:2,500,000,* BAS GEOMAP Series, Sheet 2, 20-22 British Antarctic Survey, Cambridge, England.

McKinney, W., 2010. Data structures for statistical computing in python, in *Proceedings of the 9th Python in Science Conference,* Vol. **445,** pp. 51–56.

Mieth, M., Jacobs, J., Ruppel, A., Damaske, D., Läufer, A. & Jokat, W., 2014. New detailed aeromagnetic and geological data of eastern Dronning Maud Land: implications for refining the tectonic and structural framework of Sør Rondane, East Antarctica, *Precambrian Res.,* **245,** 174–185.

Mieth, M. & Jokat, W., 2014. New aeromagnetic view of the geological fabric of southern Dronning Maud Land and Coats Land, East Antarctica, *Gondwana Res.,* **25,** 358–367.

Moorkamp, M., 2021. Joint inversion of gravity and magnetotelluric data from the Ernest-Henry IOCG deposit with a variation of information constraint, in *First International Meeting for Applied Geoscience & Energy Expanded Abstracts,* pp. 1711–1715.

Moorkamp, M., 2022. Deciphering the State of the lower crust and upper mantle with multi-physics inversion, *Geophys. Res. Lett.,* **49,** e2021GL096336.

Moorkamp, M., Heincke, B., Jegen, M., Roberts, A.W. & Hobbs, R.W., 2011. A framework for 3-D joint inversion of MT, gravity and seismic refraction data, *Geophys. J. Int.,* **184,** 477–493.

Morales-Ocaña, C., Bohoyo, F., Escutia, C., Marín-Lechado, C., Rey-Moral, C., Druet, M., Galindo-Zaldívar, J. & Maestro, A., 2023. 3D Geophysical and geological modeling of the South Orkney Microcontinent (Antarctica): tectonic implications for the Scotia Arc development, *Tectonics,* **42,** e2022TC007602.

Morlighem, M. *et al.*, 2020. Deep glacial troughs and stabilizing ridges unveiled beneath the margins of the Antarctic ice sheet, *Nat. Geosci.,* **13,** 132–137.

Morlighem, M. *et al.*, 2022. *MEaSUREs BedMachine Antarctica, Version 3 [Data Set],* NASA National Snow and Ice Data Center Distributed Active Archive Center, Boulder, CO, USA, Date Accessed 01-19-2024.

Núñez Demarco, P., Prezzi, C. & Sánchez Bettucci, L., 2020. Review of Curie point depth determination through different spectral methods applied to magnetic data, *Geophys. J. Int.,* **224,** 17–39.

Ohneiser, C., Wilson, G.S. & Cox, S.C., 2015. Characterisation of magnetic minerals from southern Victoria Land, Antarctica, *N.Z. J. Geol. Geophys.,* **58,** 52–65.

Pappa, F., Ebbing, J. & Ferraccioli, F., 2019a. Moho Depths of Antarctica: comparison of seismic, gravity, and isostatic results, *Geochem. Geophys. Geosyst.,* **20,** 1629–1645.

Pappa, F., Ebbing, J., Ferraccioli, F. & van der Wal, W., 2019b. Modeling satellite gravity gradient data to derive density, temperature, and viscosity structure of the Antarctic lithosphere, *J. geophys. Res.,* **124,** 12 053–12 076.

Pertusati, P.C., Ricci, C.A. & Tessensohn, F., 2016. *German-Italian Geological Antarctic Map Programme: the Italian contribution: a map case for 30 years of the Italian research programme in Antarctica (1985-2015),* Terra Antartica Reports No. 15, Terra Antarctica Publication.

Reitmayr, G., Korth, W., Caneva, G. & Ferraccioli, F., 2003. Gravity Survey at the Oates Coast Area, East Antarctica, during the Joint German-Italian Expedition 1999/2000, *Terra Antartica,* **10,** 97–104.

Riedel, S., Jokat, W. & Steinhage, D., 2012. Mapping tectonic provinces with airborne gravity and radar data in Dronning Maud Land, East Antarctica, *Geophys. J. Int.,* **189,** 414–427.

Roland, N.W., Henjes-Kunst, F., Kleinschmidt, G., Olesch, M., Pertusati, P.C., Schüssler, U. & Skinner, D.N.B., 2002. Geologic map of the Matusevich Glacier Quadrangle, Victoria Land, Antarctica, 1:250000, in *German-Italian Geological Antarctic Map Program (GIGAMAP),* eds Pertusati, P.C. & Tessensohn, F., Budesanstalt für Geowissenschaften und Rohstoffe (BGR).

Rossetti, F., Storti, F. & Salvini, F., 2000. Cenozoic noncoaxial transtension along the western shoulder of the Ross Sea, Antarctica, and the emplacement of McMurdo dyke arrays, *Terra Nova,* **12,** 60–66.

Ruppel, A., Jacobs, J., Eagles, G., Läufer, A. & Jokat, W., 2018. New geophysical data from a key region in East Antarctica: estimates for the spatial extent of the Tonian Oceanic Arc Super Terrane (TOAST), *Gondwana Res.,* **59,** 97–107.

Sanchez, G., Halpin, J.A., Gard, M., Hasterok, D., Stål, T., Raimondo, T., Peters, S. & Burton-Johnson, A., 2021. PetroChron Antarctica: a geological database for interdisciplinary use, *Geochem. Geophys. Geosyst.,* **22,** e2021GC010154.

Scheinert, M. *et al.*, 2016. New Antarctic gravity anomaly grid for enhanced geodetic and geophysical studies in Antarctica, *Geophys. Res. Lett.,* **43,** 600–610.

Subrahmanyam, C. & Verma, R., 1981. Densities and magnetic susceptibilities of precambrian rocks of different metamorphic grade (southern Indian Shield), *J. Geophys.,* **49**(1), 101–107.

Telford, W.M., Geldart, L.P. & Sheriff, R.E., 1990. *Applied Geophysics,* Cambridge Univ. Press.

GANOVEX Team, 1987. *Geological map of North Victoria Land, Antarctica: Explanatory notes. Geol. Jb. B 66, 7-79,* scale 1:500000, German Antarctic North Victoria Land Expedition (GANOVEX III).

Virtanen, P. *et al.*, 2020. SciPy 1.0: fundamental algorithms for scientific computing in Python, *Nat. Methods,* **17,** 261–272.

Wilson, G., Damaske, D., Möller, H.-D., Tinto, K. & Jordan, T., 2007. The geological evolution of southern McMurdo Sound—new evidence from a high-resolution aeromagnetic survey, *Geophys. J. Int.,* **170,** 93–100.

Zanutta, A. *et al.*, 2018. New geodetic and gravimetric maps to infer geodynamics of Antarctica with insights on Victoria Land, *Remote. Sens.,* **10**(10), doi:10.3390/rs10101608.